PCCP

ROYAL SOCIETY OF CHEMISTRY

PAPER

Cite this: *Phys. Chem. Chem. Phys.*, 2022, **24**, 19722

Low-frequency Raman optical activity provides insight into the structure of chiral liquids†

Pavel Michal, *[a] Josef Kapitán, [a] Jiří Kessler [b] and Petr Bouř *[bc]

Received 20th May 2022,
Accepted 28th July 2022

DOI: 10.1039/d2cp02290g

rsc.li/pccp

Vibrational frequencies of modes involving intermolecular motions in liquids are relatively small, in the Raman scattering close to the excitation frequency, and the bands may merge into a diverging uninterpretable signal. Raman optical activity (ROA) spectral shapes in this region, however, are structured more and may better reflect the nature of the studied systems. To understand the origin of the signal and its relation to the molecules, ROA spectra of six chiral neat liquids are recorded and analyzed on the basis of molecular dynamics and density functional theory computations. The theory of Raman scattering of liquids is discussed and adapted for modeling based on clusters and periodic boundary conditions. A plain cluster approach is compared to a crystal-like model. The results show that the low-frequency optical activity can be reliably modeled and related to the structure. However, momentary arrangement of molecules leads to large variations of optical activity, and a relatively large number of geometries need to be averaged for accurate simulations. The intermolecular modes are intertwined with intramolecular ones and start to dominate as the frequency goes down. The low-frequency ROA signal thus reflects the chemical composition and coupled with the modeling it provides a welcome means to study the structure and interactions of chiral liquids.

1. Introduction

Low-frequency Raman spectroscopy has been possible due to the availability of narrow wavelength optical filters and stable diode lasers, and is gaining popularity in chemical and pharmaceutical analyses.[1] It is also referred to as terahertz (THz) or low-wavenumber Raman spectroscopy. In crystals and crystalline-like polymers, it can reveal their structure, polymorphism and phonon dynamics.[2,3] Both intra and intermolecular vibrational modes provide strong Raman signal.[4] On the other hand, it is very difficult to obtain useful information from the low-frequency Raman spectrum of a liquid, because the signal is rather unstructured, unresolved, and quickly increases when the frequencies approach the excitation line.[5] Better results are obtained by optical Kerr spectroscopy exploring time dependence of the liquid polarization induced by laser pulses. In this case, low-frequency Raman spectra can be obtained by Fourier transformation techniques.[6–8]

If we look at the differential scattering of the right and left circularly polarized light, chiral liquids and solutions may provide more diverse signals than for unpolarized Raman. The bands can be both positive and negative, and are more sensitive to chemical composition and conformation.[9] Usually, only the higher-frequency region (above $\sim$400 cm^{-1}) is interpreted in terms of band assignment to the molecular structure. For a polyalanine solution in dichloroacetic acid, however, we observed a Raman optical activity (ROA) signal at 128 cm^{-1} that was about 10$\times$ stronger than the one typical for this spectroscopy.[10] Monosaccharide solutions gave rather weak low-frequency ROA,[11] whereas for several globular proteins dissolved in water the relative signal strength compared well to the big signal of polyalanine.[12] For a cryptophane molecule the intensity of the ROA band at 150 cm^{-1} significantly decreased in the presence of xenon.[13] These observations suggest that the low-frequency ROA well reacts to the structure and intermolecular interactions in the studied systems.

Also for a chiral neat liquid, 2-chloropropionitrile, we identified a strong low-frequency ROA outside the region of monomolecular fundamental modes.[14] On the basis of a cluster model the signal was assigned to intermolecular motions involving changing a distance (stretching) and mutual orientation between molecules. However, it was not clear if such a signal is related to specific intermolecular interactions, such as the ability of a molecule to make hydrogen bonds. *Ad hoc* computations based on large clusters have been quite costly in terms of computer time and memory. In the clusters most

[a] *Department of Optics, Palacký University Olomouc, 17. listopadu 12, 77146, Olomouc, Czech Republic. E-mail: michal@optics.upol.cz*
[b] *Department of Analytical Chemistry, University of Chemistry and Technology, Technická 5, 16628 Prague, Czech Republic*
[c] *Institute of Organic Chemistry and Biochemistry, Academy of Sciences, Flemingovo náměstí 2, 16610, Prague, Czech Republic. E-mail: bour@uochb.cas.cz*

† Electronic supplementary information (ESI) available: Further computational details and tests, measurement conditions, and complementary experimental data. See DOI: **https://doi.org/10.1039/d2cp02290g**

molecules remained at the surface, which did not correspond to the real situation. *Ab initio* molecular dynamics suggested for ROA relatively recently[15,16] is probably technically the most advanced way to simulate bulk phase spectra. However, it currently appears too computationally demanding.

In the present study we therefore use the cluster approach adapted to better correspond to the liquid phase, introducing a crystal-like periodicity. This enables us to investigate the low-frequency region more systematically. We also briefly review the theory of Raman scattering on liquids, which we believe has not been previously clearly linked to the cluster computational modeling. High-quality Raman and ROA experimental spectra were recorded for six chiral liquids of variable chemical structures, down to ~ 50 cm^{-1}. One of them, methyloxirane, was also investigated as an aqueous solution. Molecular dynamics is used to understand the structure of model liquids, and density functional theory is utilized for the spectroscopic properties. This computational approach seems to be fit to explain the main spectral features including low-frequency ROA signs and intensities, and thus to couple the chiral signals with the liquid structure.

2. Methods

2.1 Theory of Raman scattering in liquids

While the Rayleigh scattering[17] of gasses and liquids reflects long-range inhomogeneities in the structure, such as the radial distribution function,[18] opalescence and density fluctuations,[19,20] Raman scattering samples the structure more locally. This is because non-interacting molecules scatter Raman light in an incoherent way.[21,22]

As far as we know, there is no consistent theory comprising all quantum-mechanical and relativistic aspects of light scattering in bulk. Fortunately, the semiclassical approach based on the scattering of electromagnetic waves on individual molecules seems to provide a reasonable description of the experimental data.[9,21] To illustrate the physical basis of scattering and to justify our cluster approach, let us summarize some important relationships for the backscattering intensities. The light passing through the liquid induces time-dependent electric ($\boldsymbol{\mu}$) and magnetic ($\mathbf{m}$) dipoles and electric quadrupoles ($\boldsymbol{\Theta}$) in individual molecules, which then radiate part of the energy away. Higher moments can be neglected, because molecular dimensions are usually much smaller than the wavelength. The moments are related to the electric intensity of light through molecular polarizabilities. For example, x-polarized light of the electric field traveling along the z-direction induces a dipole moment in each molecule m[16]

$$\mu_{m\alpha} = \left(\alpha_{m\alpha x} - i\frac{k}{3}A_{m\alpha,xz} + i\frac{k}{\omega}G'_{m\alpha y}\right)E_x \tag{1}$$

where k is the wave vector, ω is the angular frequency, t is time, and α, A and G' are the electric dipole–dipole, electric dipole–quadrupole and electric dipole–magnetic dipole polarizabilities.

The induced moments are sources of scattered radiation. For Raman scattering the incident and scattered frequencies and wave vectors are close ($\omega \sim \omega'$, $k \sim k'$), so that $\Delta k = k - k' \sim 2k$ for backscattering. The electric field of light scattered from N molecules is[21]

$$E'_\alpha = \frac{\omega^2\mu_0\mu_r}{4\pi r}E_0\sum_{m=1}^{N} e^{i(\Delta k z_m - \omega t)}\left[\alpha_{m\alpha x} - \frac{ik}{3}\left(A_{m\alpha,xz} + A_{mx,\alpha z}\right) + \frac{i}{c}\left(G'_{m\alpha y} - \varepsilon_{\alpha z\gamma}G'_{mx\gamma}\right)\right] \tag{2}$$

where μ_0 and μ_r are the vacuum and relative permeabilities, and r is the distance. Unpolarized (total) Raman intensity can be associated with the S_0 Stokes parameter,

$$I_R + I_L = S_0 = E'^2_x + E'^2_y = 30\,K\sum_{m,n} e^{i\Delta k z_{mn}}\left(\alpha_{mxx}\alpha_{nxx} + \alpha_{myx}\alpha_{nyx}\right) = 30\,K\sum_{m}\left(\alpha_{mxx}\alpha_{mxx} + \alpha_{myx}\alpha_{myx}\right) \tag{3}$$

where $K = \frac{1}{30}\left(\frac{\omega^2\mu_0\mu_r}{4\pi r}E_0\right)^2$, $z_{mn} = z_m - z_n$ is the difference of positions of molecules m and n, and $I_{R/L}$ is intensity of the right/left circularly polarized light. The double sum in (3) disappears because of different phase factors of transition vibrational polarizabilities of different molecules.[20,21] For isotropic samples we can further average over molecular orientations, and express S_0 with polarizabilities related to one molecule as follows:

$$S_0 = \frac{KN}{2}\left(7\alpha_{\alpha\beta}\alpha_{\alpha\beta} + \alpha_{\alpha\alpha}\alpha_{\beta\beta}\right). \tag{4}$$

In (4) the Greek indices are related to a molecule-fixed coordinate system and the Einstein summation convention is applied here and further in the text. Adding the magnetic dipolar and electric quadrupolar parts, we similarly get the ROA intensity related to the S_3 Stokes parameter as[21]

$$I_R - I_L = S_3 = \frac{8KN}{c}\left(3\alpha_{\alpha\beta}G'_{\alpha\beta} - \alpha_{\alpha\alpha}G'_{\beta\beta} + \frac{1}{3}\,\omega\alpha_{\alpha\beta}\boldsymbol{\varepsilon}_{\alpha\gamma\delta}A_{\gamma,\delta\beta}\right) \tag{5}$$

where c is the velocity of light and $\boldsymbol{\varepsilon}$ is the antisymmetric tensor.

The single-molecule theory can be formally extended for simulations based on molecular clusters if we consider the liquid also as a sum of clusters. Any liquid volume V of N molecules can be divided into a sum of one molecule volumes v_i, volumes of molecular pairs $v_{ij} = v_i + v_j$, *etc.* (We do not consider the case when the size of the volume approaches the wavelength of the light.) For example, we can treat 3 molecules ($N = 3$) as monomers ($m = 1$) with $V = v_1 + v_2 + v_3$, dimers ($m = 2$) with $V = \frac{1}{2}(v_{12} + v_{13} + v_{23})$, where $v_{12} = v_1 + v_2$, *etc.* In general, for clusters of m molecules,

$$V = \frac{(m-1)!(N-m)!}{(N-1)!}\sum_{i_1 < i_2 < \ldots < i_m} v_{i_1 i_2 \ldots i_m}. \tag{6}$$

The total polarizability is then

$$\alpha = \frac{(m-1)!(N-m)!}{(N-1)!}\sum_{i_1 < i_2 < \ldots < i_m} \alpha_{i_1 i_2 \ldots i_m}, \tag{7}$$

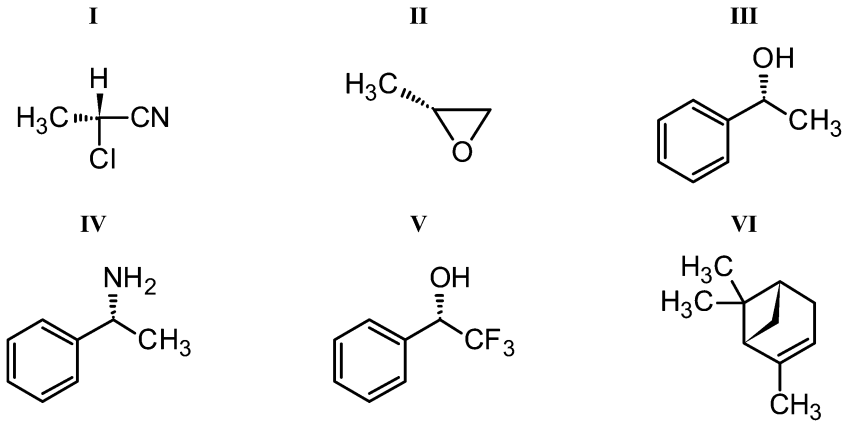

Fig. 1 Studied molecules: **I** (*R*)-2-chloropropionitrile (nitrile), **II** (*R*)-(+)-propylene oxide (methyloxirane,), **III** (*R*)-(+)-1-phenylethanol, **IV** (*R*)-(+)-α-methylbenzylamine, **V** (*S*)-(+)-α-(trifluoromethyl)benzyl alcohol, and **VI** (+)(1*R*,5*R*)-α-pinene.

where $\alpha_{i_1 i_2 \ldots i_m}$ is the polarizability of a cluster containing molecules $i_1 \ldots i_m$. The exact result is obtained for $m \rightarrow N$, when all important intermolecular interactions are included. Note that although eqn (6) and (7) may justify both the cluster and crystal-cell approaches they were not directly used in any calculation.

2.2 The periodic model

To well-represent the liquid, the clusters need to be in contact with the environment. This can be achieved using a periodic crystal-like model. Because of the periodicity, vibrational Hamiltonian H can be written as a sum over the phonon (wave) vectors $\mathbf{q}$ and atoms i within one cell only,[23]

$$H = \sum_{\mathbf{q}} \frac{1}{2} \left(\sum_i m_i \dot{x}_i^* \dot{x}_i + \sum_i \sum_j x_i^* D_{ij} x_j \right), \qquad (8)$$

where m_i and x_i are atomic masses and coordinates, and $\mathbf{D}(\mathbf{q})$ is the dynamic matrix. Only for $\mathbf{q} = 0$ we get non-zero Raman and ROA intensities. For other values signals of different elementary cells cancel out by interference. For zero wave vector,

$$D_{ij} = \sum_J f_{ij}, \qquad (9)$$

where J runs over the elementary cells containing the j-coordinate, f_{ij} are the harmonic force constants (force field). The Cartesian-normal mode transformation matrix $\mathbf{S}$ is obtained by the force field diagonalization, and the transition polarizabilities in (3) and (5) are obtained from the polarizability derivatives.[9] For example, for a fundamental transition involving the normal mode Q_J, the transition polarizability needed in eqn (4) and (5) for Raman scattering is[9]

$$\alpha(\omega, \omega') = \langle 0 | \hat{\alpha} | 1 \rangle = \sqrt{\frac{\hbar}{2\omega_J}} S_{iJ} \alpha_i, \qquad (10)$$

where ω_J is the normal mode frequency, $\hat{\alpha}$ is the polarizability dependent on atomic coordinates, α_i is a derivative with respect to coordinate i.

2.3 Spectral measurement

The six molecules studied are summarized in Fig. 1. Experimental spectra of nitrile **I** were already published.[14] Its small size, availability of both enantiomers, and relative rigidity make it a convenient testing compound. Also methyloxirane **II** is used as a convenient benchmark model for the theory.[15,24–26] A series of the ethylbenzene derivatives **III**, **IV** and **V** allows one to evaluate the spectroscopic properties of similar molecules with a mixture of inter and intramolecular low-frequency vibrational modes. (For **III** and **IV**, the very first ROA spectra were observed in 1973.[27,28]) Finally, α-pinene **VI** is an example of a non-polar molecule with weak intermolecular interactions.

Raman and ROA spectra were acquired on a custom-made ROA instrument made at Palacký University Olomouc.[14] The samples were measured in a rectangular fused silica cell of 70 μl volume, the temperature was stabilized at (20.0 ± 0.1) °C, and the back-scattering scattered circular polarization (SCP) modulation scheme was used, with a 532 nm excitation wavelength. All compounds were measured as neat liquids, and methyloxirane was additionally measured in aqueous solution at a 1 : 22 methyloxirane : H_2O molar ratio. Lower temperature (6.0 ± 0.1) °C was used for the neat and dissolved methyloxirane (boiling point at 34 °C), to prevent its evaporation. Laser powers at the sample and accumulation times are listed in Table S1 (ESI†). For **V** only one enantiomer was available, otherwise both enantiomers were measured and idealized "(*R*–*S*)/2" ROA spectra for the *R*-forms are presented. A fluorescence background in the Raman signal of **V** caused by impurities was subtracted using the asymmetric least squares algorithm,[29,30] with the asymmetry parameter 1×10^{-4} and smoothness 8.5×10^4. Experimental intensities are given as the number of detected electrons per excitation energy in a wavenumber interval (e^- cm J^{-1}).

2.4 Computations

Molecular dynamics (MD) was performed using the Tinker program.[31] Some computations were repeated or complemented using the Amber software,[32] which allowed for a more

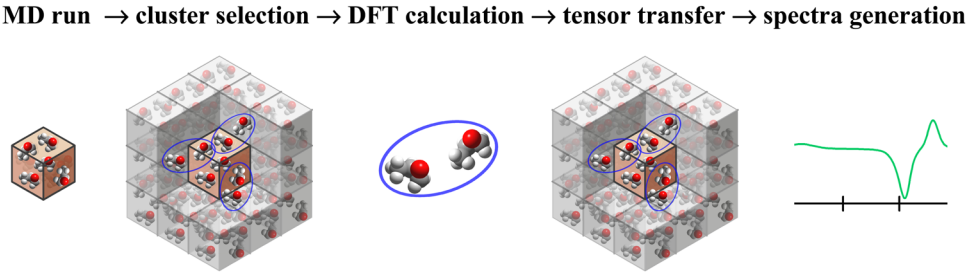

Fig. 2 Simulations of the spectra by the default crystal-like model. Intermolecular interactions within the periodic elementary cell (the brown/middle cube) and towards its environment were simulated for molecular pairs, in an arbitrary 27 cube "supercube". The pair parameters (force field, intensity tensors) were transferred back to the supercube, and the spectra were simulated using the periodic boundary conditions.

extensive parallelization and time saving, providing nearly identical results to Tinker. The OPLSAA force field was used,[33] with periodic boundary conditions, production run of 10 ns, 1 fs integration time, *NVT* ensembles, and temperature of 298 K. For methyloxirane the OPLSAA force field was modified to reproduce bond lengths and angles calculated by Gaussian[34] at the B3LYP/aug-cc-pVTZ/COSMO(THF) approximation level. Bigger periodic cubic boxes (about 40 Å a side) were used for investigations of the radial distribution functions, smaller ones (Table S2, ESI† containing 10 molecules) were used to generate many snapshots and their spectra.

Vibrational frequencies and spectral intensities were calculated using the Gaussian program and the B3PW91[35]/6-31G**/COSMO[36]/GD3BJ[37,38] method. Even 10 molecules in the box were too many for a direct calculation of a large number of snapshots needed for convergence. Therefore, smaller clusters were made, by default containing two close molecules, presumably comprising the strongest intermolecular interaction within the periodic box and 26 neighboring boxes (Fig. 2). The geometries of the pairs or larger clusters were partially optimized in the normal mode coordinates.[39–41] Modes with frequencies below 225 cm^{-1} (or below 100i cm^{-1} when imaginary, $i = \sqrt{-1}$) were fixed, and harmonic frequencies were calculated at the same level as the geometries. For Raman and ROA intensity tensors the rDPS[42] basis set was combined with the B3PW91/6-31G**/COSMO/GD3BJ force field. The rDPS basis set has been recommended for ROA because of a good balance between the computational demands and quality of the results.[42,43] For example, rDPS polarizability derivatives were calculated about 2–3 times faster than for a larger 6-31++G** basis set, giving almost identical results (Fig. S1, ESI†). The rDPS basis set alone is not suitable for the frequencies, underestimating them by about 40–50 cm^{-1} (*cf.* Fig. S1c and d, ESI†). A simpler BPW91 functional was tried

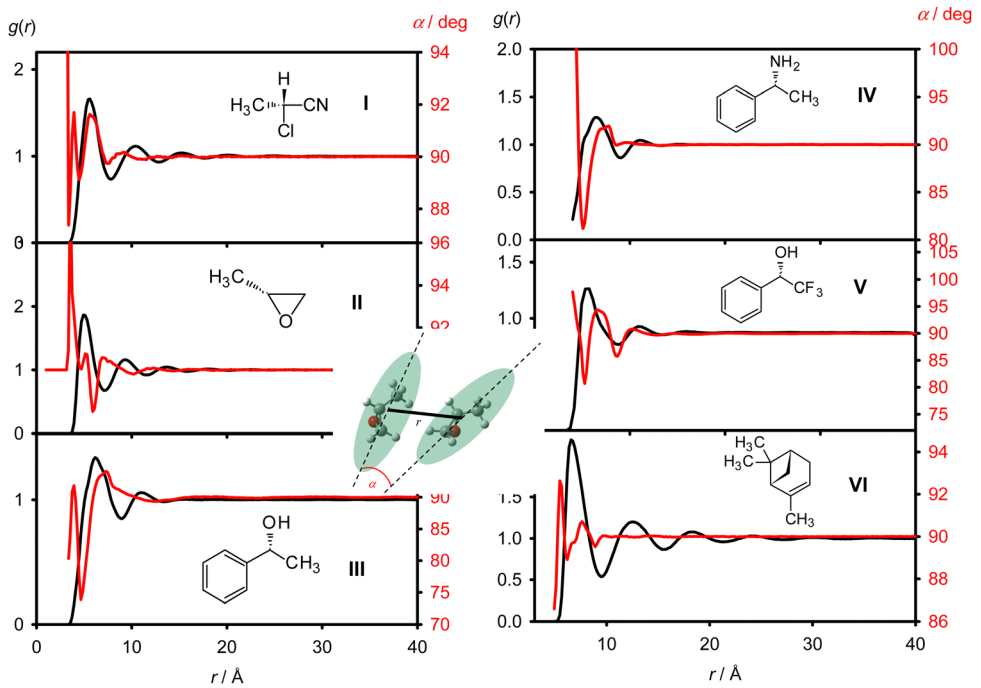

Fig. 3 Radial distribution functions $g(r)$ (black line) and average angle α (red) between two molecules as a function of the distance. The angle is defined according to the main moments of inertia as indicated in the inset.

and gave qualitatively similar results to B3PW91; also the influence of the GD3BJ dispersion correction was rather minor (Fig. S2, ESI†).

Vibrational parameters (force field and polarizability derivatives) thus obtained for the smaller clusters were transferred back to the 3 × 3 × 3 supercube (Fig. 2) using the Cartesian coordinate transfer (CCT).[44,45] From the resultant force field we obtained the dynamic matrix (eqn (9)) and calculated the Raman and ROA intensities for each transition i (I_i, eqn (4) and (5)). Smooth spectra were obtained as

$$S(\omega) = \sum_i I_i \left[1 - \exp\left(-\frac{\omega_i}{kT}\right)\right]^{-1} \left[4\left(\frac{\omega - \omega_i}{\Delta}\right)^2 + 1\right]^{-1}, \quad (11)$$

where ω_i is the transition frequency, k is the Boltzmann constant, Δ = 10 cm^{-1}, and temperature T = 298 K. The magnitude of the bandwidth (Δ) approximately corresponds to the experimental resolution and thus facilitates comparison to the experiment.

For testing, as an alternative to the default crystal-like model (part 2.2), larger clusters comprising one molecule and its first solvation sphere were also used for spectral generation, following ref. 14. Selected from MD with the bigger periodic boxes, the clusters were partially optimized and the spectra calculated following the procedure described above for the crystal model. Finally, we also experimented with the supercube (Fig. 2), which we used not only for the generation of the dynamic matrix in the crystal model, but directly as a cluster. Although these two cluster models miss the continuous character of the liquid, as shown below they also reproduce some of the features observed experimentally.

3. Results and discussion

3.1 Molecular dynamics simulations

The radial distribution functions (RDFs) calculated from MD provide insight into the range of intermolecular interactions in the studied liquids (Fig. 3). All exhibit a clear maximum of the first solvation sphere, at 5.6 Å (**I**), 5.1 Å (**II**), 6.2 Å (**III**), 6.5 Å (**IV**),

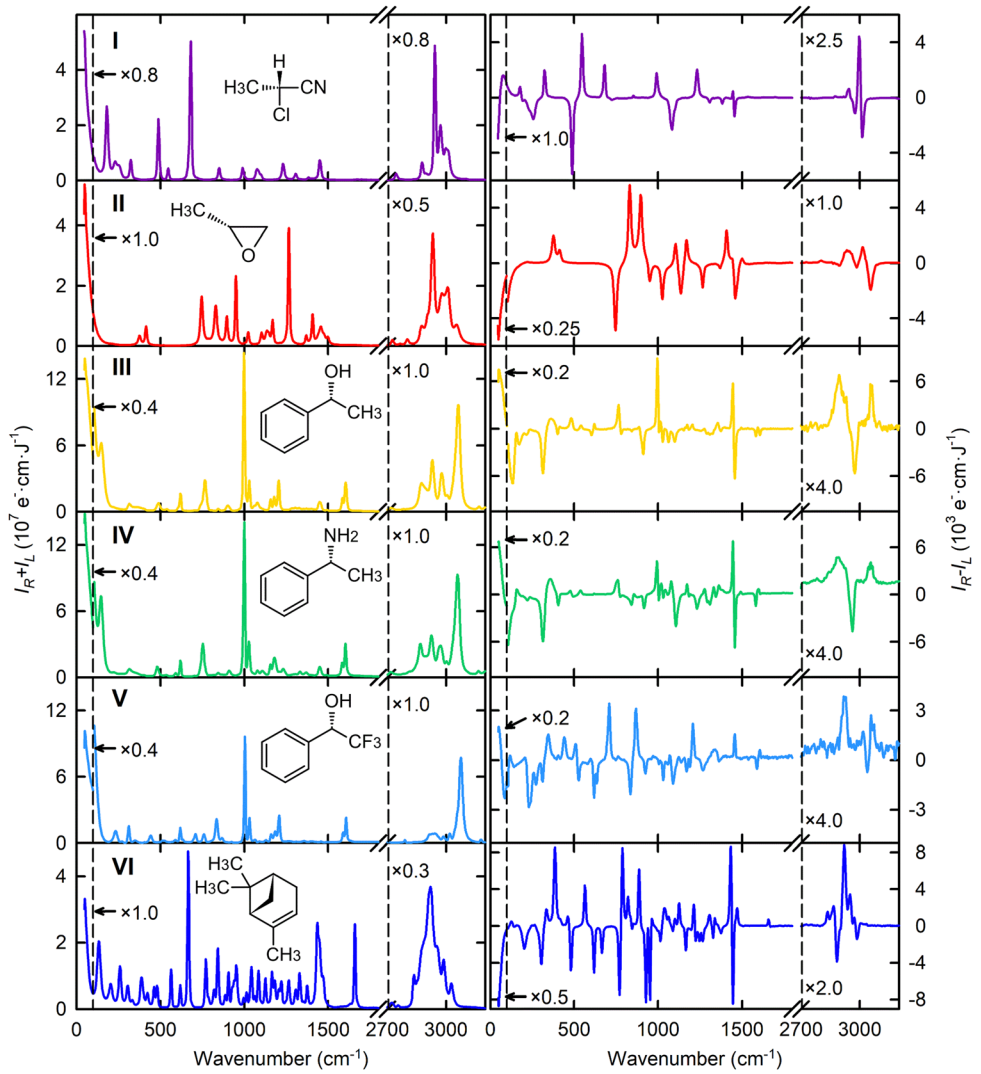

Fig. 4 Experimental Raman and ROA spectra of the six neat chiral liquids.

6.0 Å (**V**), and 6.5 Å (**VI**). Other maxima associated with higher solvation spheres are obviously less pronounced, although the fifth solvation sphere maximum of α-pinene at ~30 Å is still visible. Also the RDFs of the other two "rigid" molecules, methyloxirane and nitrile, are structured up to a relatively long distance, whereas for the ethylbenzene derivatives the structure is nearly destroyed after the second maximum.

The angle α between the main axes of molecular moments of inertia (red lines in Fig. 3) averages to 90° for distant non-interacting molecules. At shorter distances molecules interact and adopt energetically favorable mutual orientations. The case when $\alpha \neq 90°$ thus indicates that an additional source of chirality in the solution exists, apart from the absolute configuration of individual molecules. This can potentially contribute to low-frequency ROA. We can see that for the rigid molecules (nitrile, methyloxirane, and α-pinene) α does not deviate by more than 3° from the 90° average, except for the closest distance limit. Ethylbenzenes **III–V** adapt their shapes upon more contact and the deviations from 90° are bigger, with an extreme value of 15° for alcohol **III**.

For **III–V** the molecular flexibility can also be judged from the dependencies of the electronic energy (B3PW91/6-311++G**/COSMO) on the conformation of the phenyl, hydroxy and amine groups (Fig. S3, ESI†). All three molecules prefer the polar OH or NH groups pointing out of the phenyl plane ($\varphi \sim 100°$). The OH/NH_2 groups are relatively freely rotating, with energy minima with ψ at about ±60° and 180°. The potential energy barriers between the minima are within 1–2 kcal mol^{-1} for **III** and **V**, and higher (3 kcal mol^{-1}) for **IV**. For **III** and **IV**, the calculated potential energy surfaces are consistent with a previous study.[28] However, the distributions of MD conformers (black dots in Fig. S3, ESI†) follow the DFT results only approximately. We explain this by the possibility of the molecules to form hydrogen bonds in MD, which is only partially simulated by the COSMO continuum solvent model.[46]

3.2 Experimental spectra

The experimental Raman and ROA spectra recorded in the whole range (~50–3200 cm^{-1}) for the six compounds are plotted in Fig. 4. When available, enantiomers gave opposite

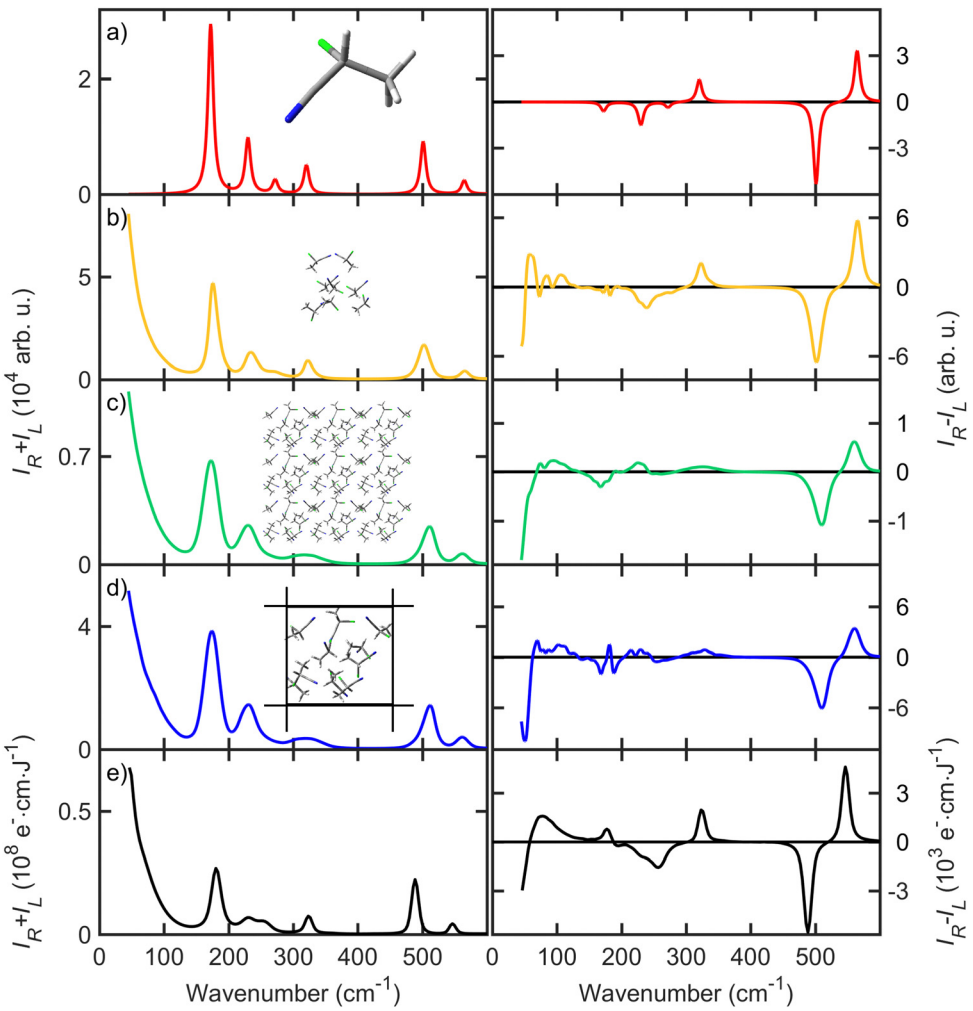

Fig. 5 Raman and ROA nitrile (**I**) spectra calculated with different models: (a) single molecule, (b) small cluster/all interactions, (c) large cluster/pair interactions, (d) periodic crystal/pair interactions (*cf.* Fig. 2), and (e) experimental spectrum. For b–d 200 MD snapshots were averaged.

ROA, suggesting a very low level of instrumental artifacts (Fig. S4, ESI†). The region within 1800–2700 cm^{-1} is not shown because there is only one fundamental band, nitrile C≡N stretching. ROA signal at the CH stretching region (>2700 cm^{-1}) is relatively weak, but the shapes therein are also characteristic for individual molecules. The strong "scissoring" signal of compounds containing methyl groups (±ROA couplet at ~1450 cm^{-1}) is missing for **V**. We also see the bigger sensitivity of ROA spectra compared to Raman scattering; compounds **III–V** have very similar Raman spectra, but only some ROA features are alike.

Normalized circular intensity difference ratios (CID = ROA/Raman, Fig. S5, ESI†) in the CH stretching region are rather small (maximum of ~1×10^{-4} for **I**, 3×10^{-5} for **VI**, *etc.*). In the lower frequencies (<2000 cm^{-1}) CIDs are higher, up to ~9×10^{-4} for the smaller molecules and ~2×10^{-3} for **VI**. At the 50 cm^{-1} instrumental limit CIDs are rather small again, **II** and **VI** giving the highest values of 4×10^{-4} and 6×10^{-4}, respectively. The CID parameters are important, for example, for determining the reliability of the measurement and for comparison to the simulations. Note, however, that the experimental values cannot be determined too accurately due to the fluorescent background in the Raman spectrum.

Below we focus on the lowest-wavenumber region, where all liquids have strong ROA even as the frequency approaches 50 cm^{-1}. For **I** and **III–V**, there are also strong bands at ~90 cm^{-1}. These have opposite sign to the intensity at the 50 cm^{-1} limit. The six compounds studied suggest that the low frequency signal is not related to a particular molecular property, such as size, hydrophobicity, or the ability to make hydrogen bonds. This was also observed for a few other chiral liquids not shown here.

3.3 Strategies for spectra modeling

Fig. 5 compares spectra of **I** simulated with (a) one nitrile molecule, (b) molecular clusters, (c) bigger cluster with pair interactions only, and (d) the periodic crystal model; (e) is the experimental spectrum. The low-frequency intermolecular signal is obviously missing in the single molecule spectra (a). Also the inhomogeneous broadening of the bands within 150–350 cm^{-1} simulated by the arbitrary Lorentzian band is not realistic. The other models based on MD do provide the intermolecular signal with a correct ROA sign pattern, (positive at ~80 cm^{-1}, negative close to 50 cm^{-1}). Minor spectral features are difficult to judge due to the limited precision of the calculations and limited experimental resolution.

The MD, however, except for the small cluster model (b), overestimates the broadening of the 242 and 325 cm^{-1} bands. As discussed previously[47] generation of the spectra using the instantaneous normal mode approximation and partial optimization[39] of MD geometries is a rather empirical procedure, which may contribute to this inconsistency. The widths of the intramolecular bands within 150–300 cm^{-1} are simulated qualitatively correctly. The periodic crystal-like model (d) is technically the most advanced one and avoids the surface cluster effects, but it comprises pair molecular interactions only. Some experimental

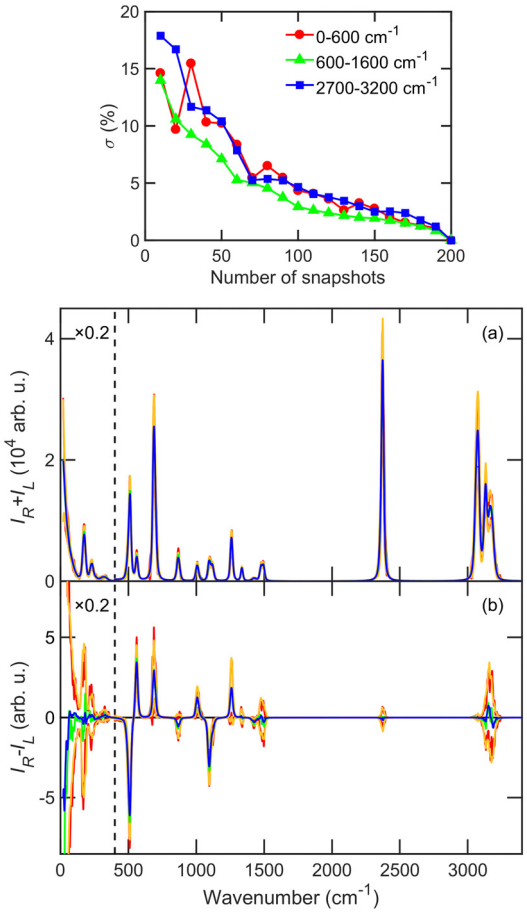

Fig. 6 Nitrile, (top) dependence of the ROA spectral average error ($\sigma = \int|S_i - S_f|d\upsilon / \int|S_f|d\upsilon$, S_i and S_f are the partial and final average) on the number of averaged snapshots, for three spectral regions, and (bottom) Raman and ROA nitrile spectra averaged from 20 (green) and 200 (blue) MD snapshots; standard deviations ($s = \sqrt{(N-1)^{-1}\sum(S_i - \bar{S})^2}$) at each point are plotted using red (20) and orange (200) lines.

features, like the relatively monotonic increase of the ROA intensity between 250 and 90 cm^{-1}, are therefore better reproduced with the smaller clusters containing more intermolecular interactions (b). The large cluster model (c) seems to give the worst results. Nevertheless, we see that all the cluster models are able to reasonably well reproduce also the intermolecular low-frequency ROA signal. Spectra simulated with the crystal-like model (d) for all compounds in a broad wavenumber range are summarized in Fig. S6 (ESI†). This model is also used as a default below, unless said otherwise.

A serious problem limiting the precision of the computations is a large number of MD snapshots that need to be averaged for low-frequency ROA. The convergence is documented at the top of Fig. 6. We can see the ROA spectral error as dependent on the number of averaged snapshots, in the low (0–600 cm^{-1}), middle (600–1600 cm^{-1}) and CH stretching (2700–3200 cm^{-1}) regions. The 200-snapshot average is taken as a reference. The low-frequency ROA signal converges more slowly than within 600–1600 cm^{-1}. About 100 snapshots need to be averaged to push the error below 5%. For Raman (not shown)

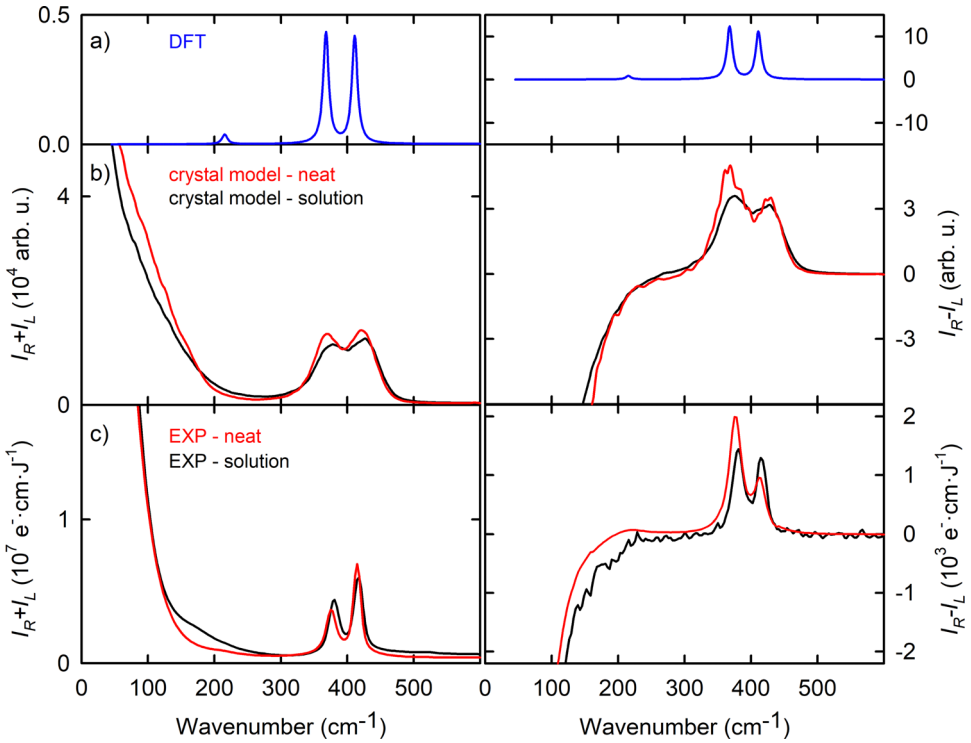

Fig. 7 Raman and ROA spectra of neat methyloxirane and its water solution: (a) single molecule computation, (b) crystal model, and (c) experiment.

about 10 snapshots would be enough. Somewhat surprising is a slow convergence of the CH ROA signal, similar to that for the low-frequency region. This can perhaps be explained by the extended coupling of the CH stretching motion with other modes.[48]

At the bottom of Fig. 6 Raman and ROA spectra of the nitrile are plotted as calculated from 20 and 200 MD snapshots. About 20 snapshots already provide many spectral features observed also experimentally, but the positive 80 cm^{-1} ROA maximum, for example, appears only after the whole set is included. The ROA sensitivity to a momentary MD geometry is also reflected by the standard deviations plotted using red and orange lines in Fig. 6. These clearly become extreme for low-frequency ROA. For bands above 400 cm^{-1} the 20 and 200 snapshot averages are nearly the same. The convergence problem makes the computation expensive. Note that one snapshot already involves some averaging over molecular orientations. For example, if there are 10 molecules in the elementary cell (Fig. 2) we need to calculate force fields for about 50 different pairs of molecules to comprise at least the main intermolecular interactions within this cell and to neighboring ones.

On one nitrile snapshot, we also tested the convergence of the spectra with respect to the number of molecules taken in the clusters to calculate the force field (Fig. S7, ESI†). Increasing this value is quite computationally demanding: one elementary cell of 10 molecules provides 10 monomers, roughly 50 dimers of close molecules, 390 trimers, 1300 tetramers, *etc.* In the trial snapshot, accounting for three and four-molecule interactions seems to produce some additional ROA features around 100 cm^{-1} compared to the pairs; however, this is not observed experimentally and likely disappears during the averaging. The low-frequency ROA signal for the monomers is caused by differences of equilibrium and MD geometries, which is an inherent restriction of our method, but may be significantly reduced during further averaging. Increasing the number of molecules in one elementary cell (*i.e.*, size of the MD box) did not seem to bring an improvement and 10 molecules in the box thus seem to be sufficient for a converged result (Fig. S8, ESI†).

3.4 Methyloxirane solution and vibrational mode analysis

Interestingly, neat methyloxirane gave nearly the same low-frequency ROA signal as its water solution, and this result could be reproduced by the crystal model (Fig. 7). To achieve a reasonable convergence, however, more MD snapshots (1000) were needed for the solution than for the neat liquids (200). In the experiment, compared to the neat liquid, the water solution has an extra Raman and ROA signal around 180 cm^{-1}, most probably originating in the methyl group rotation. Also the two fundamental bands of skeletal/bending modes around 400 cm^{-1} are shifted by ~3 cm^{-1} to the right. These details are partially reproduced by the calculations (band shift by ~8 cm^{-1}), and the overall reasonable agreement between the experiment and the modeling allows us to better understand the low-frequency ROA, primarily stemming from translational and rotational-like motions of individual chiral molecules. This observation is consistent with Fig. 3 showing that two methyloxirane molecules are not much mutually oriented even at the closest distances. In other words, a methyloxirane molecule senses the neighboring one primarily as spheres, and their shape or chirality plays a secondary role.

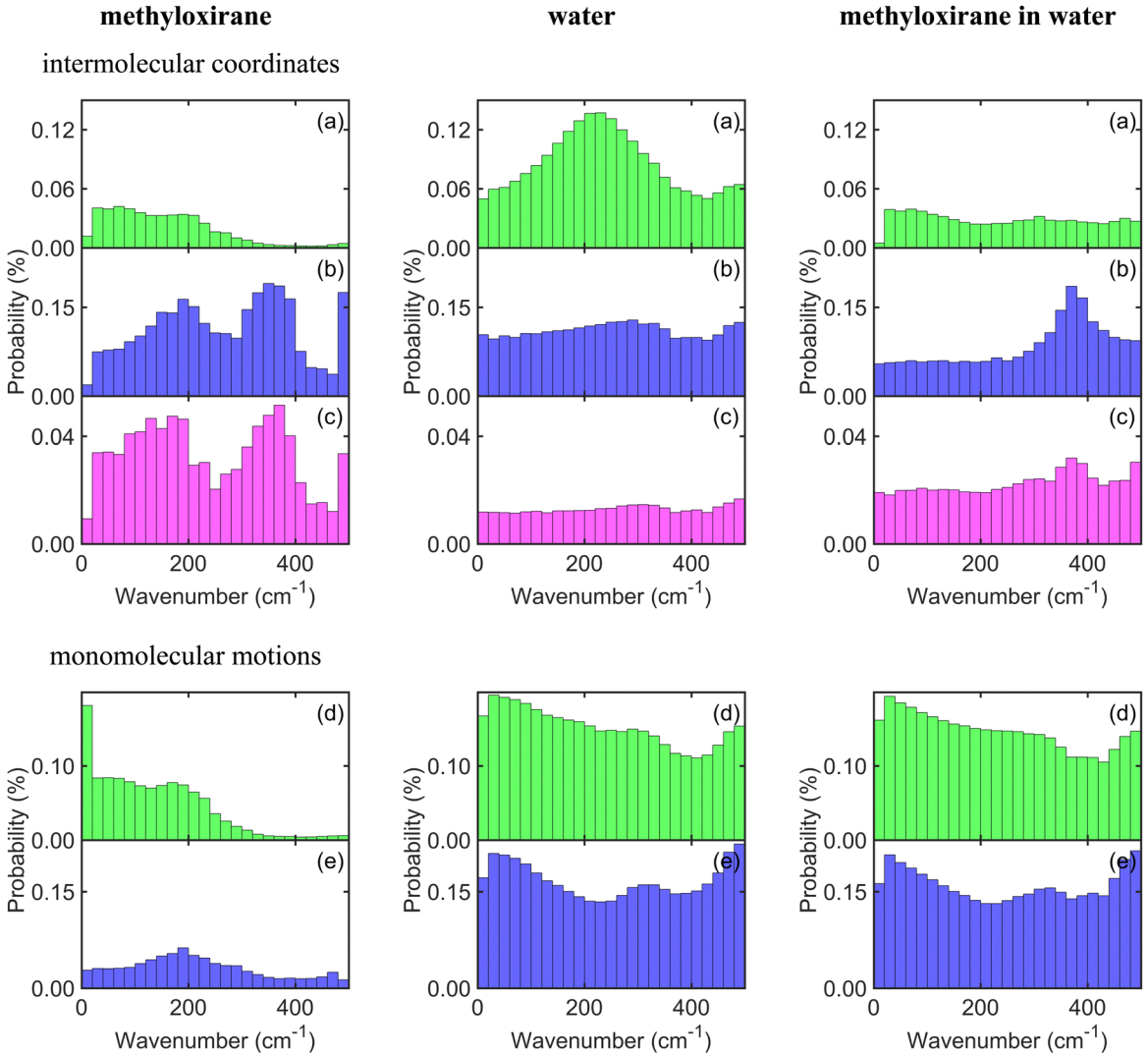

Fig. 8 Relative vibrational potential energies of intermolecular motions related to two (stretching (a), bending (b), torsion (c)) and one (translations (d), rotations (e)) molecules, for neat methyloxirane, water and a mixture.

In a different way we try to understand the low-frequency vibrations introducing intermolecular coordinates, or translations and rotations of one molecule.[14] The corresponding potential energy distributions (PEDs, see the definition in Fig. S9, ESI†) are plotted in Fig. 8. Note that redundant sets of the coordinates were created automatically and their PEDs are not unique. Nevertheless, in the current set we see that intermolecular motions formally contribute differently to the vibrational energy in water, methyloxirane, and the mixture. In pure water, a clear band around 220 cm^{-1} for the stretching (a) is developed. In neat methyloxirane the stretching starts to contribute in the lowest frequencies only, and the contribution is smoothed out in the mixture. The bending (b) and twisting (c) modes are most structured in neat methyloxirane, reflecting the more complicated shape of the molecule. At this level, it is difficult to interpret the histograms in more detail, but the broadness of the probability distributions does not suggest that a specific interaction would be responsible for the low-frequency ROA, and is thus consistent with the similarity of the neat liquid and solution spectra.

3.5 III–VI, theory *vs.* experiment

For the other molecules (**III–VI**) the vibrational potential energy distributions (Fig. S9, ESI†) are more complex than for water or methyloxirane. The intermolecular modes are more intertwined with low-frequency intramolecular motions, such as rotations of the phenyl, methyl, hydroxyl, trifluoromethyl and amine groups (*cf.* Table S3, ESI† with the normal mode assignment). The histogram distributions for **III–V** are quite similar, showing higher contributions of molecular translations, intermolecular stretchings and rotations with decreasing frequency. For α-pinene **VI** the stretching also becomes important for the lowest frequencies, while the intermolecular bending and twisting modes are more mixed with intramolecular ones and formally thus contribute even close to 500 cm^{-1}.

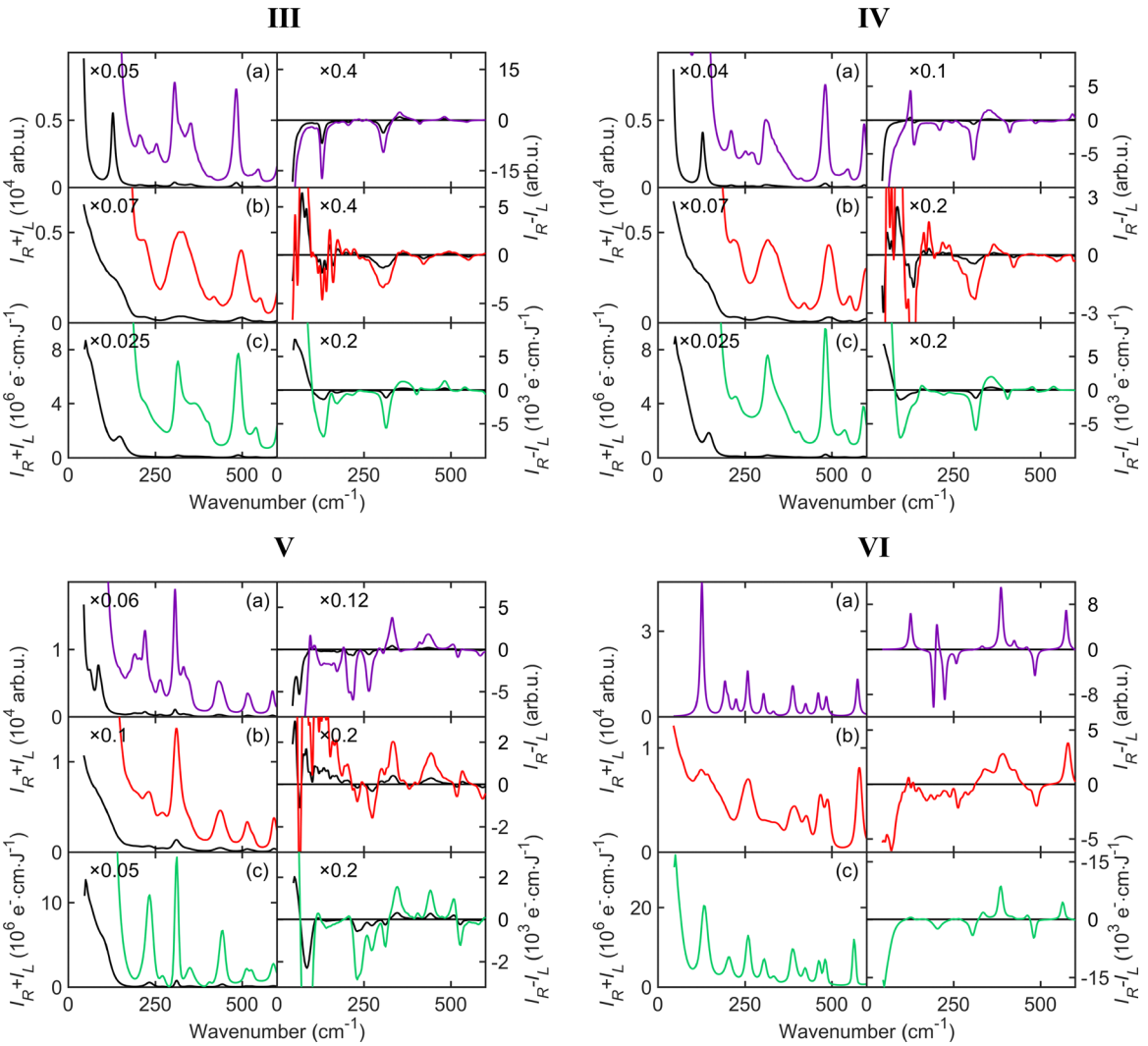

Fig. 9 Raman and ROA spectra of **III–VI** (a) simulation of one molecule (**III–V** conformer averaging, **VI** – minimum only), (b) the crystal model, and (c) the experiment.

Raman and ROA spectra of **III–VI** simulated with one molecule including averaging over the potential energy surface and the crystal-like approach are compared to those of the experiment in Fig. 9. These "more complicated" molecules possess many low-frequency intra(mono)molecular fundamental vibrational modes, and the single molecule simulation reasonably well describes some Raman and ROA spectral features down to $\sim$200 cm^{-1}. However, in the lowest frequency region the multimolecular crystal model performs better. In particular, it correctly gives the ROA sign as the frequency approaches 50 cm^{-1}. Least satisfying is the simulation for the fluorine-containing compound **V**, probably because of inaccuracy of the OPLSAA force field. For example, the crystal model often gives the fundamental bands too broad and wrong signs of the 507 and 528 cm^{-1} ROA bands of **V**. In spite of these minor inconsistencies, we find it important that we can at least semi-quantitatively understand the observed data in terms of molecular structure and interactions. The modeling technology is also flexible and open to improvement when a bigger computer power becomes available.

4. Conclusions

We developed a crystal-like computational protocol that allowed us to analyze in detail low-frequency ROA spectra of six example chiral liquids. The results show that the signal is a complicated function of molecular structure that can be understood only on the basis of spectral simulations. The low-frequency modes are not too specific; nevertheless, the analysis of the vibrational potential energy suggests that for small rigid molecules (α-pinene, chloropropionitrile, and methyloxirane) the low-frequency signal comes primarily from molecular translations and rotations. For more flexible molecules the molecular/intermolecular low-frequency modes are mixed with monomolecular fundamentals. Very similar spectra were

observed for neat methyloxirane and its water solution; this rather surprising observation could be reproduced with the crystal model and provided a phenomenological insight into the low-frequency chirality. Although the precision of the simulations is limited due to available computer power, they provide a sound theoretical basis to interpret the observed spectra and can be systematically improved in the future. The low-frequency ROA spectroscopy thus provides an interesting window into the world of chiral molecules, their structure and interactions, and can bring about useful knowledge about their behavior for biology and industry.

Conflicts of interest

J. Kapitán and P. Michal are involved in commercialization of the ROA technique. The other authors have no interest to declare.

Acknowledgements

This work was supported by the Czech Grant Agency (20-10144S, 22-04669S), the Ministry of Education (CZ.02.1.01/0.0/0.0/16_019/0000729 and e-INFRA CZ LM2018140), and student grant of the Palacký University Olomouc (IGA_PrF_2022_001).

References

1 K. Bērziņš, S. J. Fraser-Miller and K. C. Gordon, *Int. J. Pharm.*, 2021, **592**, 120034.
2 P. Ranzieri, A. Girlando, S. Tavazzi, M. Campione, L. Raimondo, I. Bilotti, A. Brillante, R. G. Della Valle and E. Venuti, *ChemPhysChem*, 2009, **10**, 657–663.
3 S. Yamamoto, Y. Morisawa, H. Sato, H. Hoshina and Y. Ozaki, *J. Phys. Chem. B*, 2013, **117**, 2180–2187.
4 J. J. Lazarević, S. Uskoković-Marković, M. Jelikić-Stankov, M. Radonjić, D. Tanasković, N. Lazarević and Z. V. Popović, *Spectrochim. Acta, Part A*, 2014, **126**, 301–305.
5 L. A. Blatz, in *Raman Spectroscopy*, ed. H. A. Szymanski, Springer, Boston, MA, 1970, DOI: **10.1007/978-1-4684-3027-1_4**.
6 Q. Zhong and J. T. Fourkas, *J. Phys. Chem. B*, 2008, **112**, 15529–15539.
7 E. W. Castner and M. Maroncelli, *J. Mol. Liq.*, 1998, **77**, 1–36.
8 D. A. Turton, J. Hunger, A. Stoppa, A. Thoman, M. Candelaresi, G. Hefter, M. Walther, R. Buchner and K. Wynne, *J. Mol. Liq.*, 2011, **159**, 2–8.
9 L. Nafie, *Vibrational optical activity: Principles and applications*, Wiley, Chichester, 2011.
10 S. Yamamoto, S. Ishiro, J. Kessler and P. Bouř, *Phys. Chem. Chem. Phys.*, 2021, **23**, 26501–26509.
11 V. Palivec, P. Michal, J. Kapitán, H. Martinez-Seara and P. Bouř, *ChemPhysChem*, 2020, **21**, 1272–1279.
12 J. Kessler, J. Kapitán and P. Bouř, *J. Phys. Chem. Lett.*, 2015, **6**, 3314–3319.
13 T. Buffeteau, D. Pitrat, N. Daugey, N. Calin, M. Jean, N. Vanthuyne, L. Ducasse, F. Wien and T. Brotin, *Phys. Chem. Chem. Phys.*, 2017, **19**, 18303–18310.
14 P. Michal, R. Čelechovský, M. Dudka, J. Kapitán, M. Vůjtek, M. Berešová, J. Šebestík, K. Thangavel and P. Bouř, *J. Phys. Chem. B*, 2019, **123**, 2147–2156.
15 M. Brehm and M. Thomas, *J. Phys. Chem. Lett.*, 2017, **8**, 3409–3414.
16 Y. Yang, J. Cheramy, M. Brehm and Y. Xu, *ChemPhysChem*, 2022, **23**, e202200161.
17 L. Rayleigh, *Philos. Mag.*, 1899, **47**, 375–384.
18 L. I. Komarov and I. Z. Fischer, *Soviet Phys. JETP*, 1963, **16**, 1358–1361.
19 A. Einstein, in *Collected Papers of Albert Einstein, The Swiss Years: Writings 1909–1911*, ed. M. J. Klein, A. J. Kox, J. Renn and R. Schulmann, Princeton U. P., Princeton, 1994, vol. 3, pp. 231–249.
20 A. G. Rojo and P. R. Berman, *Am. J. Phys.*, 2010, **78**, 94–101.
21 L. D. Barron, *Molecular Light Scattering and Optical Activity*, Cambridge University Press, Cambridge, UK, 2004.
22 D. Pestov, G. O. Ariunbold, X. Wang, R. K. Murawski, V. A. Sautenkov, A. V. Sokolov and M. O. Scully, *Opt. Lett.*, 2007, **32**, 1725–1727.
23 L. Piseri and G. Zerbi, *J. Mol. Spectrosc.*, 1968, **26**, 254–261.
24 F. Lipparini, F. Egidi, C. Cappelli and V. Barone, *J. Chem. Theory Comput.*, 2013, **9**, 1880–1884.
25 T. D. Crawford and K. Ruud, *ChemPhysChem*, 2011, **12**, 3442–3448.
26 J. Šebestík and P. Bouř, *J. Phys. Chem. Lett.*, 2011, **2**, 498–502.
27 L. D. Barron, M. P. Bogaard and A. D. Buckingham, *J. Am. Chem. Soc.*, 1973, **95**, 603–605.
28 J. Kapitán, C. Johannessen, P. Bouř, L. Hecht and L. D. Barron, *Chirality*, 2009, **21**, E4–E12.
29 P. Eilers and H. Boelens, Leiden University Medical Centre report, 2005.
30 S. Baek, A. Park, Y. Ahn and J. Choo, *Analyst*, 2015, **140**, 250–257.
31 J. W. Ponder, *Tinker, Software Tools for Molecular Design*, Washington University School of Medicine, Saint Louis, 3.8 edn, 2000.
32 D. A. Pearlman, D. A. Case, J. W. Caldwell, W. S. Ross, T. E. Cheatham, S. Debolt, D. M. Ferguson, G. Seibel and P. A. Kollman, *Comput. Phys. Commun.*, 1995, **91**, 1–41.
33 R. C. Rizzo and W. L. Jorgensen, *J. Am. Chem. Soc.*, 1999, **121**, 4827–4836.
34 M. J. Frisch, G. W. Trucks, H. B. Schlegel, G. E. Scuseria, M. A. Robb, J. R. Cheeseman, G. Scalmani, V. Barone, G. A. Petersson and H. Nakatsuji, *et al.*, *Gaussian 16 Rev. A.03*, Gaussian, Inc., Wallingford, CT, 2016.
35 A. D. Becke, *J. Chem. Phys.*, 1993, **98**, 1372–1377.
36 A. Klamt, V. Jonas, T. Burger and J. C. W. Lohrentz, *J. Phys. Chem. A*, 1998, **102**, 5074–5085.
37 S. Grimme, J. Antony, S. Ehrlich and H. Krieg, *J. Chem. Phys.*, 2010, **132**, 154104.
38 S. Grimme, S. Ehrlich and L. Goerigk, *J. Comput. Chem.*, 2011, **32**, 1456–1465.

39 P. Bouř and T. A. Keiderling, *J. Chem. Phys.*, 2002, **117**, 4126–4132.
40 P. Bouř, *Collect. Czech. Chem. Commun.*, 2005, **70**, 1315–1340.
41 P. Bouř, *Qgrad*, Academy of Sciences, Prague, 2006.
42 G. Zuber and W. Hug, *J. Phys. Chem. A*, 2004, **108**, 2108–2118.
43 K. Ruud and J. Thorvaldsen, *Chirality*, 2009, **21**, E54–E67.
44 P. Bouř, J. Sopková, L. Bednárová, P. Maloň and T. A. Keiderling, *J. Comput. Chem.*, 1997, **18**, 646–659.
45 S. Yamamoto, X. Li, K. Ruud and P. Bouř, *J. Chem. Theory Comput.*, 2012, **8**, 977–985.
46 P. Bouř, D. Michalík and J. Kapitán, *J. Chem. Phys.*, 2005, **122**, 144501.
47 J. Hudecová, K. H. Hopmann and P. Bouř, *J. Phys. Chem. B*, 2012, **116**, 336–342.
48 J. Hudecová, V. Profant, P. Novotná, V. Baumruk, M. Urbanová and P. Bouř, *J. Chem. Theory Comput.*, 2013, **9**, 3096–3108.